J. Mech. Phys. Solids 167 (2022) 105023

Contents lists available at ScienceDirect

Journal of the Mechanics and Physics of Solids

journal homepage: www.elsevier.com/locate/jmps

Formation of surface wrinkles and creases in constrained dielectric elastomers subject to electromechanical loading

Chad M. Landis [a,b,*], Rui Huang [a], John W. Hutchinson [c]

[a] Department of Aerospace Engineering and Engineering Mechanics, University of Texas, Austin, TX, United States
[b] Oden Institute for Computational Engineering and Science, University of Texas, Austin, TX, United States
[c] School of Engineering and Applied Sciences, Harvard University, Cambridge, MA, United States

ARTICLE INFO

Keywords:
Dielectric elastomer
Instability
Bifurcation
Numerical analysis

ABSTRACT

This paper investigates issues that have arisen in experimental and theoretical studies of the stability of a dielectric elastomeric layer bonded to a stiff substrate and subject to a voltage difference across the top and bottom conducting surfaces of the layer. The role of equi-biaxial pre-stretch of the layer prior to bonding to the substrate is a central factor in the investigation. The focus is the competition between wrinkling and creasing and how this competition is affected by pre-stretch. A finite element model of the system is employed to generate wrinkling bifurcation and advanced post-bifurcation solutions in the form of localized modes, either crease-like or groove-like depending on the pre-stretch. The constitutive model includes elastic compressibility, but the formulation produces accurate solutions for nearly incompressible materials which coincide with the neo-Hookean solid in the incompressible limit. The numerical simulations reveal that localized crease solutions exist at voltages below the critical voltage for wrinkling bifurcation for equi-biaxial pre- stretches below about 2.4. In this range, the wrinkling bifurcation is highly unstable, creasing rather than wrinkling can be expected, and a discontinuous transition is predicted with a finite energy barrier that may be overcome due to the presence of surface defects. With an equi-biaxial pre-stretch greater than 2.4, a continuous transition is predicted with no energy barrier, forming a localized groove due to nonlinear interactions among the unstable wrinkling modes.

1. Introduction

Electromechanical instability has been recognized as a mode of failure for dielectric elastomer membranes subject to increasing voltage (Stark & Garton 1955; Plante & Dubowsky 2006), which limits the amount of energy conversion by dielectric elastomers in practical applications (Zhao and Suo 2007; Koh et al., 2011). A series of groundbreaking experiments on pre-stretched dielectric elastomeric layers bonded to stiff substrates and subject to a voltage difference across top and bottom conducting surfaces revealed that the uniformity of the layers gave way to localized creasing-like instabilities as the voltage difference was increased (Kofod et al., 2003; Wang et al. 2011a, 2011b; Wang and Zhao, 2013). These observations occurred only a few years after a clear understanding of the competition between wrinkling and localized creasing had emerged for elastomeric layers subject to compression. Hohlfeld (2008) and Hohlfeld and Mahadevan (2011), followed up by Hong et al. (2009), showed that localized surface crease solutions existed at

* Corresponding author.
E-mail address: landis@utexas.edu (C.M. Landis).

https://doi.org/10.1016/j.jmps.2022.105023
Received 8 March 2022; Received in revised form 2 July 2022; Accepted 5 August 2022
Available online 6 August 2022

compression levels lower than Biot (1963) critical compression for bifurcation into sinusoidal surface wrinkles. Moreover, the finite strain crease solutions existed at arbitrarily small sizes, assuming scale effects such as surface tension could be ignored, implying that the surface imperfections required to trigger the creasing instabilities could similarly be arbitrarily small. This new understanding finally explained the observation that creasing, not wrinkling, was the dominant mode of surface instability for compressed elastomeric materials (Tanaka et al. 1987; Gent and Cho, 1999). Many others have also contributed to the understanding of the competition between wrinkling and creasing in elastomers subject to mechanical compression (Cao and Hutchinson, 2011; Cai et al, 2012; Diab et al., 2013).

The initial theoretical work on the electromechanical surface instabilities mainly focused on the localized creasing solutions and the creasing threshold voltage, i.e., the lowest imposed voltage difference at which the crease solutions exist (Wang et al. 2011a; Park et al. 2013). The numerical analysis of the finite strain creasing solution is challenging for several reasons, especially because the wavelength of the wrinkling mode is indeterminate and the solution path from the uniform state to the creased state is highly nonlinear and unstable. The present paper addresses these issues in the investigation of the competition between wrinkling and creasing. Confusion exists in the literature surrounding the critical voltage at which bifurcation into surface wrinkling modes occurs. A recent paper by Hutchinson (2021) presenting the voltage at wrinkling bifurcation as a function of pre-stretch for neo-Hookean layers was in error and has been corrected by Hutchinson et. al (2022). For an incompressible neo-Hookean layer with ground state shear modulus, μ, dielectric permittivity, ε, and an equi-biaxial pre-stretch, λ_0, the critical voltage difference across the layer, V_W, at the onset of short wavelength sinusoidal, plane-strain wrinkling modes is given by

$$\sqrt{\frac{\varepsilon}{\mu}}\left(\frac{V_W}{h}\right) = \sqrt{\frac{\lambda_0^9+\lambda_0^6+3\lambda_0^3-1}{\lambda_0^4\left(\lambda_0^3+1\right)}} = \lambda_0\sqrt{1+\lambda_0^{-6}\left(\frac{3-\lambda_0^{-3}}{1+\lambda_0^{-3}}\right)} \tag{1.1}$$

where h is the thickness of the incompressible layer in the pre-stretched state prior to bifurcation. With no pre-stretch, $\lambda_0 = 1$, this reduces to $V_W/h = \sqrt{2\mu/\varepsilon}$, in agreement with an early result of Huang (2005). At a pre-compression of $\lambda_0 = 0.6662$, Eq. (1.1) is satisfied with, $V_W = 0$, corresponding to Biot's prediction for surface wrinkling under equi-biaxial compression (Biot, 1963). The surface wrinkling condition (1.1) underpins the crease analysis in that it provides an upper bound to the voltage at which unstable crease formation is expected and because wrinkling bifurcations from the uniform state can evolve to creases.

The objective of the present study is to uncover creasing solutions as a function of pre-stretch and to provide numerically accurate results for the threshold voltage above which stable creases can exist. The highly nonlinear behavior of crease formation is discussed. The primary emphasis is on the behavior of imperfection-free layers. However, limited results for one class of imperfections are provided revealing the strong sensitivity to small imperfections of the critical voltage required to trigger a crease. It will be seen that the difference between the crease threshold and the wrinkling bifurcation diminishes with increasing pre-stretch and appears to vanish at pre-stretches above about $\lambda_0 = 2.4$. With an equi-biaxial pre-stretch greater than 2.4, nonlinear interactions among the unstable wrinkling modes lead to groove-like localization.

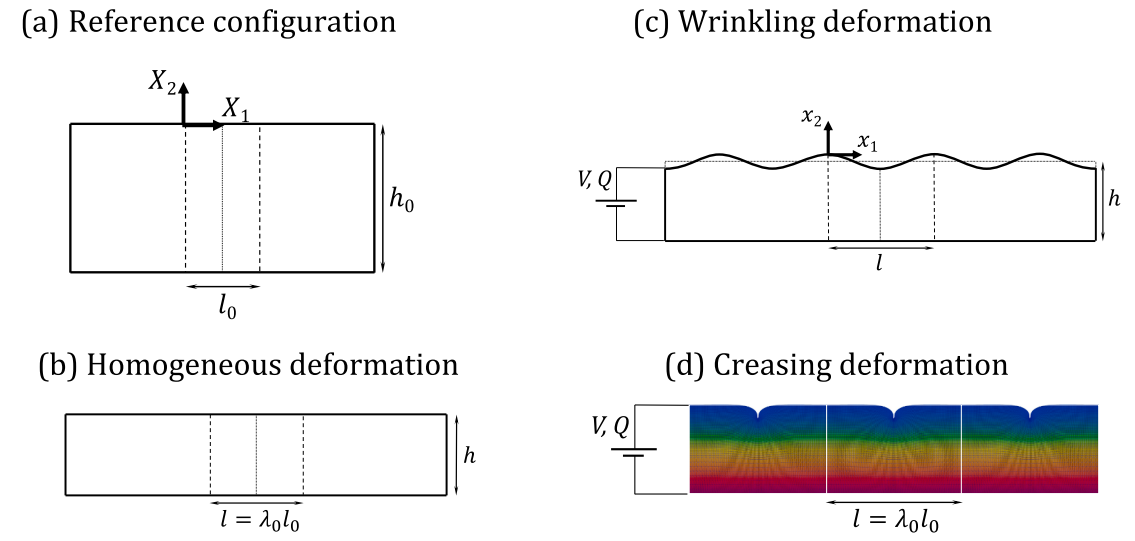

Fig. 1. (a) The reference configuration of a dielectric elastomer film of thickness h_0, prior to the application of pre-stretch or electrical loading. (b) Homogeneous deformation by an equi-biaxial pre-stretch λ_0. After the film is pre-stretched, it is then bonded to a rigid conducting substrate such that upon the application of electrical loading it is constrained from lateral expansion/contraction along the bottom surface. During electrical loading a voltage drop V is applied across the top and bottom conducting surfaces of the film, and a resulting charge Q is exchanged. Above a critical electromechanical loading, the homogeneous deformation becomes unstable and bifurcation takes place to form either (c) periodic surface wrinkles or (d) periodic creases.

2. Critical condition for the onset of surface wrinkling

Fig. 1 illustrates the reference and deformed configurations of a dielectric elastomer layer. Coordinates in the reference configuration (Fig. 1a) are denoted X_I, and those in the current configuration are denoted x_i. Note that the coordinates in the current configuration can also be written in terms of the displacement as $x_i = \delta_{iJ}X_J + u_i$. The deformation gradient is $F_{iJ} = \frac{\partial x_i}{\partial X_J} = x_{i,J} = \delta_{iJ} + u_{i,J}$, and the nominal electric field is $E_I = -\frac{\partial \phi}{\partial X_I} = -\phi_{,I}$, where ϕ is the electric potential and δ_{iJ} is the Kronecker delta relating the current configuration to the reference configuration. The dielectric elastomer is assumed to be nearly incompressible, modeled by a compressible form of the free energy function. Two forms of the free energy functions are used in this work:

$$W(F,E) = \frac{\mu}{2}(F_{iJ}F_{iJ} - 3 - 2\ln J) + \frac{1}{2}\left(\kappa - \frac{2\mu}{3}\right)(J-1)^2 - \frac{\varepsilon}{2}JF^{-1}_{Ki}F^{-1}_{Li}E_K E_L, \tag{2.1}$$

or

$$W(F,E) = \frac{\mu}{2}\left(J^{-\frac{2}{3}}F_{iJ}F_{iJ} - 3\right) + \frac{\kappa}{4}\left(J^2 - 1 - \ln J^2\right) - \frac{\varepsilon}{2}JF^{-1}_{Ki}F^{-1}_{Li}E_K E_L. \tag{2.2}$$

Here, μ and κ are the usual shear modulus and bulk modulus when the material is subjected to infinitesimal deformation, ε is the dielectric permittivity, and $J = \det(F_{iJ})$ is the determinant of the deformation gradient. Note that the elastic parts of both of these model free energies reduce to the neo-Hookean model in the incompressible limit as $\frac{\kappa}{\mu} \to \infty$. The governing equations of mechanical equilibrium and charge balance, i.e. Gauss' law, are given as,

$$P_{Ji,J} + b_i = 0 \ \text{ in } V_0 \ \text{ and } P_{Ji}N_J = t_i \ \text{ on } S_0 \tag{2.3}$$

$$D_{I,I} = q \ \text{ in } V_0 \ \text{ and } D_I N_I = -\omega \ \text{ on } S_0 \tag{2.4}$$

where $P_{Ji} = \frac{\partial W}{\partial F_{iJ}}$ is the first Piola-Kirchhoff stress, $D_I = -\frac{\partial W}{\partial E_I}$ is the nominal electric displacement, t_i is the surface traction, b_i is the body force, ω is the surface charge density and q is the body charge density. V_0 and S_0 denote the volume and bounding surface of the domain in the reference configuration. Note that the constitutive equations for the stress and electric displacement are provided above in the identifications of these quantities.

Fig. 1b illustrates a homogeneous deformation of the dielectric elastomer layer subject to an equi-biaxial pre-stretch λ_0 but no electrical loading. This in-plane stretch also causes a change in the film thickness from h_0 to h. Electrical loading by voltage (V) or charge (Q) is then applied to this state of the layer. The in-plane equi-biaxial stretch provides a relationship between an in-plane length l in the deformed configuration and that in the reference configuration l_0 as $l = \lambda_0 l_0$. The electrical loading will cause an additional homogeneous deformation of the film for the compressible case (but not for the incompressible case). The homogeneous deformation becomes unstable at a critical loading and bifurcates to inhomogeneous deformations in form of either wrinkling or creasing, as illustrated by Fig. 1c and d. A linear perturbation analysis was conducted recently by Hutchinson (2021) to predict the critical condition for the onset of the wrinkling bifurcation for an incompressible neo-Hookean layer. A subtle error in the analysis has been identified and corrected by Hutchinson et al. (2022). Here, we briefly review the derivation of the critical electromechanical conditions to cause wrinkling of the dielectric elastomer film, assuming a compressible form of the free energy function in Eq. (2.1) or (2.2). Wrinkling is defined in this work as a periodic sinusoidal deformation that extends over the entire surface (Fig. 1c), as opposed to the highly localized deformations that are associated with creasing (Fig. 1d). The critical conditions for creasing will be determined numerically in Section 4.

Here, the entire analysis is carried out in the reference configuration prior to the application of the pre-stretch or electrical loading. Analytical solutions for both forms of the free energy functions given in Eqs. (2.1) and (2.2) have been obtained for arbitrary bulk to shear modulus ratios, κ/μ, and arbitrary levels of the equi-biaxial pre-stretch, λ_0. The general procedure for generating these solutions follows that described in Eqs. (2.1)-(2.19) but with the perturbed solutions for the current coordinates taking the form, $x_i = \lambda_0\delta_{iJ}X_J + (\lambda_2 - \lambda_0)\delta_{i2}X_2 + \alpha u_i(X_1, X_2)$, instead of the simpler form shown in Eq. (2.5) for $\lambda_0 = 1$. The details of Eqs. (2.7)-(2.19) are then altered accordingly. For simplicity, we present the analytical result for the free energy function from Eq. (2.1) and for the case of no pre-stretch ($\lambda_0 = 1$). The effect of pre-stretch on the critical condition has been discussed in previous works (Hutchinson, 2021; Hutchinson et al., 2022) for the case of an incompressible neo-Hookean material.

We look for perturbed solutions about a homogeneous state given by,

$$x_i = \delta_{iJ}X_J + (\lambda_2 - 1)\delta_{i2}X_2 + \alpha u_i(X_1, X_2) \tag{2.5}$$

$$\phi = \frac{V}{h_0}(X_2 + h_0) + \alpha\varphi(X_1, X_2) \tag{2.6}$$

where V is the voltage applied to the top surface at $X_2 = 0$, λ_2 is the homogeneous stretch in the normal direction, $\alpha u_i(X_1, X_2)$ is the perturbed displacement field, $\alpha\varphi(X_1, X_2)$ is the perturbed electric potential field, and α is a dimensionless small parameter. Before perturbation, the traction-free condition on the top surface governs the homogeneous deformation state which satisfies the equation,

$$\frac{\varepsilon}{2}\left(\frac{V}{h_0}\right)^2+\left(\kappa-\frac{2}{3}\mu\right)\lambda_2^2(\lambda_2-1)+\mu\lambda_2\left(\lambda_2^2-1\right)=0 \tag{2.7}$$

The equilibrium equations and Gauss' law are expanded to order α^1 and yield equations governing the perturbed fields,

$$\frac{V}{\lambda_2 h_0}u_{2,11}+\frac{V}{\lambda_2^3 h_0}u_{2,22}-\varphi_{,11}-\frac{1}{\lambda_2^2}\varphi_{,22}=0 \tag{2.8}$$

$$\left[\left(\kappa-\frac{2}{3}\mu\right)+\mu\left(1+\frac{1}{\lambda_2^2}\right)\right]u_{2,22}+\mu u_{2,11}+\left[\lambda_2\left(\kappa-\frac{2}{3}\mu\right)+\frac{\mu}{\lambda_2}\right]u_{1,21}=0 \tag{2.9}$$

$$\left[\lambda_2^2\left(\kappa-\frac{2}{3}\mu\right)+2\mu\right]u_{1,11}+\mu u_{1,22}+\left[\lambda_2\left(\kappa-\frac{2}{3}\mu\right)+\frac{\mu}{\lambda_2}\right]u_{2,21}=0 \tag{2.10}$$

These equations are subject to the voltage and traction-free boundary conditions on the surface of the film,

$$\varphi(X_1,0)=0 \tag{2.11}$$

$$\left[\frac{\mu}{\lambda_2}-\left(\kappa-\frac{2}{3}\mu\right)(\lambda_2-1)-\frac{\varepsilon V^2}{2h\lambda_2^2}\right]u_{2,1}(X_1,0)+\mu u_{1,2}(X_1,0)=0 \tag{2.12}$$

$$\frac{\varepsilon V}{h_0\lambda_2^2}\varphi_{,2}(X_1,0)+\left[\left(\kappa-\frac{2}{3}\mu\right)+\frac{\mu}{\lambda_2}+\frac{\mu(\lambda_2-1)^2}{\lambda_2^2}-\frac{\varepsilon V^2}{h_0\lambda_2^3}\right]u_{2,2}(X_1,0)+\left(\kappa-\frac{2}{3}\mu\right)(1+\lambda_2)u_{1,1}(X_1,0)=0 \tag{2.13}$$

Taking the wavenumber of the wrinkling solution to be unity, and the wavelength of the wrinkle to be much smaller than h, the solution to these equations is,

$$\varphi(X_1,X_2)=\frac{V}{h_0\lambda_2}\{u_2(X_1,X_2)-U_2(1-A)\exp[\lambda_2 X_2]\cos(X_1)\} \tag{2.14}$$

$$u_2(X_1,X_2)=U_2\{\exp[X_2]-A\exp[pX_2]\}\cos(X_1) \tag{2.15}$$

$$u_1(X_1,X_2)=-U_2\left\{\frac{1}{\lambda_2}\exp[X_2]-\frac{A\lambda_2}{p}\exp[pX_2]\right\}\sin(X_1) \tag{2.16}$$

where

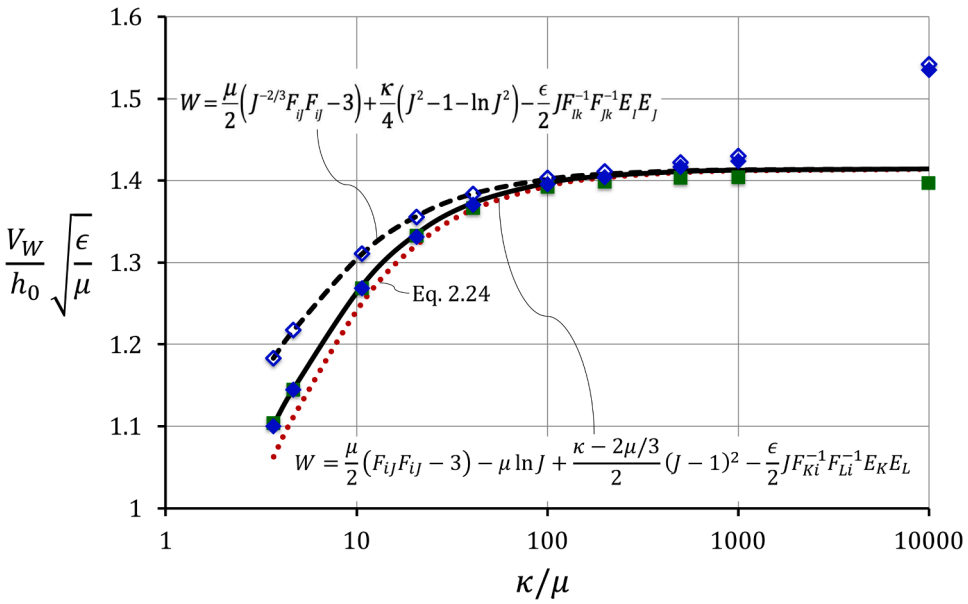

Fig. 2. The critical voltage V_W for the onset of wrinkling. The solid and dashed black lines are the analytical solutions for the two different forms of the free energy function as shown. The red dotted line (●) is the analytic solution by Huang (2005) given in Eq. (2.24). The green squares (■) are the finite element solutions for the Q1EI4 element (bottom free energy function only), and the blue diamonds (◆ and ◇) are the finite element solutions for the Q1P0 element that is detailed in this work and is used for the creasing simulations.

$$p = \lambda_2 \sqrt{\frac{2\mu + \left(\kappa - \frac{2}{3}\mu\right)\lambda_2^2}{\mu + \left(\kappa + \frac{1}{3}\mu\right)\lambda_2^2}} \tag{2.17}$$

$$A = \frac{\varepsilon\left(\frac{V}{h_0}\right)^2 + 2\lambda_2\left[\lambda_2(\lambda_2 - 1)\left(\kappa - \frac{2}{3}\mu\right) - 2\mu\right]}{\varepsilon\left(\frac{V}{h_0}\right)^2 + 2\lambda_2\left[(\lambda_2 - 1)\left(\kappa - \frac{8}{3}\mu\right) + (\lambda_2 - 1)^2\left(\kappa - \frac{5}{3}\mu\right) - 2\mu\right]} \tag{2.18}$$

The critical condition for the onset of the wrinkling instability results from an eigenvalue problem required to satisfy the boundary conditions (2.11-2.13), yielding

$$V = h_0 \sqrt{\frac{-b - \sqrt{b^2 - 4ac}}{2a}} \tag{2.19}$$

where

$$a = \frac{\varepsilon^2}{4}\left(1 - p\lambda_2^{-2}\right) \tag{2.20}$$

$$b = \varepsilon\left[\lambda_2^2(\lambda_2 - 1)\left(\kappa - \frac{2}{3}\mu\right) - 2\mu\lambda_2 - p(\lambda_2 - 1)\left(\kappa - \frac{2}{3}\mu\right) + p\left(\lambda_2^2 + \lambda_2 - 1 + \lambda_2^{-1}\right)\mu\right] \tag{2.21}$$

$$c = \lambda_2^2\left[\lambda_2(\lambda_2 - 1)\left(\kappa - \frac{2}{3}\mu\right) - 2\mu\right]^2 - p\left[\lambda_2(\lambda_2 - 1)\left(\kappa - \frac{2}{3}\mu\right) - \left(\lambda_2^2 + 1\right)\mu\right]^2 \tag{2.22}$$

The critical voltage is then obtained by combining Eq. (2.19) with Eq. (2.7). The results of this calculation for the critical voltage for an elastomer film with no pre-stretch ($\lambda_0 = 1$) are shown in Fig. 2 as the solid black line. In the limit of an incompressible material, we have $\kappa \to \infty$, $p \to 1$, $a \to 0$, $b \to 2\varepsilon\mu$, $c \to -4\mu^2$, and the critical condition becomes,

$$\frac{V}{h_0} = \sqrt{\frac{2\mu}{\varepsilon}} \text{ as } \kappa \Big/ \mu \to \infty \tag{2.23}$$

In addition to the solution for this free energy function, the analytic solution for the second free energy function of Eq. (2.2) is shown in Fig. 2 as the dashed black line for comparison. The red dots (●) on Fig. 2 are the analytical solution from the early work of Huang (2005), who assumed a linearly elastic material (see Appendix B for details) and obtained a closed form expression for the critical voltage as a function of Poisson's ratio, $\nu = (3\kappa - 2\mu)/(6\kappa + 2\mu)$:

$$\frac{V}{h_0} = \frac{3 - 6\nu + 4\nu^2}{4(1 - \nu)^{\frac{5}{2}}}\sqrt{\frac{\mu}{\varepsilon}} \tag{2.24}$$

Note that this result is closest to the full finite deformation analytic result that uses the free energy function of Eq. (2.1). For a nearly incompressible material (i.e., $\kappa/\mu \geq 1000$), the critical voltage for wrinkling is well predicted by Eq. (2.23), regardless of the free energy function.

3. Finite element methods for wrinkling and creasing

The weak form of the boundary value problem is derived from variations of the functional in Eq. (3.1) as outlined by Simo and Armero (1992). Furthermore, we will focus on the implementation of the Q1P0 element, which is an isoparametric quadrilateral element that uses linear interpolations for the displacement fields and piecewise constants for the pressure p, and dilatational θ fields. The functional is defined as,

$$\Pi(u_i, \phi, \theta, p) = \int_{V_0} \overline{W}(\overline{F}_{iJ}, E_I) dV_0 + \int_{V_0} p(J - \theta) dV_0 - \int_{V_0} b_i u_i - q\phi dV_0 - \int_{S_0} t_i u_i - \omega\phi dS_0 \tag{3.1}$$

Note the introduction of a new deformation gradient $\overline{F}_{iJ}$, which is defined as, $\overline{F}_{iJ} = \theta^{\frac{1}{3}}\widehat{F}_{iJ}$ where $\widehat{F}_{iJ} = J^{-\frac{1}{3}}F_{iJ}$. It will be shown in the following that the variation of Π with respect to p dictates that the dilatational variable θ takes on the average of J within a given element. Hence $\overline{F}_{iJ}$ replaces the point-wise distribution of J within the element uniformly with its average for the Q1P0 element. $\overline{W}(\overline{F}_{iJ}, E_I)$ is then simply the free energy of one of the forms defined previously in Eq. (2.1) or (2.2) evaluated at $\overline{F}_{iJ}$. However, when taking derivatives of the free energy we must recognize that $\overline{F}_{iJ}$ depends on both θ and u_i. Setting the first variations of Π to zero results in the following consequences for the Q1P0 element (recall that both p and θ are constant within a given element). The variation with respect to p yields

$$\delta p : \int_{V_0} (J - \theta) dV_0 = 0 \tag{3.2}$$

which then provides the result that θ is the volume average of J within each element, namely

$$\theta = \frac{1}{V_0}\int_{V_0} J dV_0 \tag{3.3}$$

Variation with respect to θ then provides the determination of p as,

$$\delta\theta: \; p = \frac{1}{V_0}\int_{V_0} \frac{1}{3}\frac{\partial \overline{W}}{\partial \overline{F}_{iJ}}\frac{\overline{F}_{iJ}}{\theta} dV_0 \tag{3.4}$$

However, this information is not needed for the solution of the system and a reduced variational principle can be formulated solely in terms of the displacements and electrical potential by recognizing that the variation with respect to θ can be written in terms of the variations of the displacement gradient as,

$$\delta\theta = \frac{1}{V_0}\int_{V_0} J F^{-1}_{Ji}\delta u_{i,J} dV_0 \tag{3.5}$$

The reduced variational principle is then

$$\delta\Pi = 0: \int_{V_0}\frac{\partial \overline{W}}{\partial \overline{F}_{iJ}}\delta\overline{F}_{iJ} + \frac{\partial \overline{W}}{\partial E_I}\delta E_I dV_0 = \int_{V_0} b_i\delta u_i - q\delta\phi dV_0 + \int_{S_0} t_i\delta u_i - \omega\delta\phi dS_0. \tag{3.6}$$

Details of the derivation of the residual vector and tangent stiffness based on this variational principle are given in Appendix A. The creasing problem exhibits strongly unstable behavior and so we also note that in some cases additional viscous and inertial terms were added to the formulation with the sole purpose of allowing the system to evolve towards equilibrium. Once the system was sufficiently close to equilibrium these extra terms were removed, i.e. set to zero, and the equilibrium solutions satisfying the formulation outlined above and in Appendix A were then obtained.

In addition to the Q1P0 element that was developed by Simo and Armero (1992), we also studied finite element formulations based on the standard displacement-electric potential formulation, and interestingly, a two-dimensional Hu-Washizu Q1EI4 mixed element that has been studied by Auricchio et al. (2013) for the mechanical problem. Mueller-Hoeppe et al. (2009) provide an excellent presentation of the analogous three-dimensional element, which can be simplified for the two-dimensional case. For this work, the element was enhanced to include standard electromechanical coupling. For mechanical loading only, Auricchio et al. (2013) showed that this element shows promise for nearly incompressible materials. Unfortunately, we found that with the standard electromechanical enhancement, this element exhibited hourglassing instabilities for the electrically induced creasing problem. We believe that additional non-standard electromechanical enhancements of this element may prove to be valuable, but such investigations are beyond the scope of this work. Results for the wrinkling problem using the Q1EI4 mixed element will be included in the results that follow, but for the sake of brevity the details of the formulation are not given here and the reader is referred to Mueller-Hoeppe et al. (2009) for additional details.

4. Numerical results and discussion

4.1. Wrinkling

The blue diamonds (◆) and green squares (■) in Fig. 2 are the finite element results for the onset of wrinkling using the Q1P0 and Q1EI4 elements, respectively. Note that the wrinkling solution decays exponentially from the deformed surface in the X_2 direction with a length-scale proportional to the wavelength. As noted previously (Hutchinson, 2021; Hutchinson et al., 2022), the critical voltage for wrinkling becomes nearly a constant for $l/h < 1$ as the short-wave limit. As in the Biot problem, all wrinkling wavelengths ($l/h < 1$) become critical at the same loading level. Hence, for these calculations, a rectangular domain of height h and half-wavelength $l/2 = h/10$ was simulated. The displacements and electric potential of the bottom surface of the domain are fixed to zero. The vertical sides of the domain are restricted from horizontal displacement, traction-free tangentially, and charge-free, i.e. the normal component of the nominal electric displacement is zero. Electrically the top surface is loaded under charge-control, by enforcing the uniform voltage using multi-point constraints. All of the electric potential degrees of freedom on the top surface are tied to the lead node located at $(0, h)$. A generalized electrical force is then applied to this lead node which is equivalent to the opposite of the total charge residing on the entire top surface. The mechanical boundary conditions on the top surface are more complex than simply traction-free. To be able to simulate wrinkling, the creasing mode of deformation must be suppressed. To accomplish this the following multi-point constraint is applied to the vertical component of the mechanical displacements on the top surface nodes, u_2^N:

$$u_2^N = \frac{u_2^L + u_2^R}{2} + \frac{u_2^L - u_2^R}{2}\cos\left(\frac{2\pi X_1}{l}\right) \tag{4.1}$$

where u_2^L is the vertical displacement of the leader node at $(0, h)$ and u_2^R is the vertical displacement of the other leader node at $(l/2, h)$. The first term must be included to allow the compressible film to change thickness freely as voltage is applied to the surface. The second term is then used along with equal magnitude and oppositely directed forces on the two leader nodes to probe the generalized applied moment as a function of the deformation amplitude, $(u_2^L - u_2^R)/2$, for the surface. Note that no imperfection is used in these calcu-

lations. Instead, charge (or equivalently voltage) is applied to the top surface up to a fixed level and then the generalized moment is applied. The critical voltage for the onset of wrinkling is then determined at the charge/voltage when the slope of the moment-amplitude response goes to zero. The slope is positive below the critical voltage and is negative above the critical voltage.

The results of this simulation process are shown in Fig. 2 for both the Q1P0 elements and the Q1EI4 elements. We note that both element types perform reasonably well up to $\kappa/\mu \approx 1000$. This corresponds to a Poisson's ratio of $\nu = 0.4995$. However, beyond $\kappa/\mu \approx 1000$ the Q1P0 element begins to yield results that are significantly above the analytical prediction of the critical voltage. On the other hand, the results for the Q1EI4 elements begin to decrease below the analytical result for larger values of κ/μ, but to a much milder extent than the increase seen for the Q1P0 element. This suggests that the Q1EI4 element may be superior. However, for creasing simulations the Q1EI4 element exhibited an hourglassing instability at the critical load when creasing was not suppressed. Hence, the Q1P0 elements are used in the simulations of creasing, with a bulk to shear modulus ratio of $\kappa/\mu = 1000$. This value is taken for the rest of this work focusing on the nearly incompressible behavior, for which the numerical results from the Q1P0 elements are reasonably close to the analytical results for the onset of wrinkling.

4.2. Creasing

Park et al. (2013) have previously studied the creasing problem with similar numerical methods. The distinction in this work is on a more detailed study of the equilibrium states, both stable and unstable, associated with creasing. Additionally, the effects of pre-stretch, distance between creases, and conducting defects are also studied. Fig. 3 shows a solution for a creased state along with the quantities that are used to study creasing. The downward displacement of the crease tip is denoted by u and the downward force on the crease tip, which is used to study the unstable branch of the creasing response, is denoted by F. The area of the surface of the periodic domain is $A = lt$, where t is the out-of-plane thickness, and Q is the total charge residing on the surface of one periodic domain. Note that for the wrinkling simulations the wrinkling wavelength and the length of the periodic domain are equal and are both denoted by the length l. After the presentation of results for perfect films, a small conducting channel of length a that is not able to open mechanically is introduced within the calculations. As with the wrinkling calculations, only a half-periodic domain is modeled in the creasing calculations, with symmetry boundary conditions on the left ($x_1 = 0$) and the right ($x_1 = l/2$). We first study the cases with a relatively small domain having an aspect ratio of $l/h = 2$, where the pre-stretch $\lambda_0 = l/l_0$ varies. The effects of the domain size on the creasing behavior are discussed afterwards. The choice of this periodic domain size was motivated by the work of Park et al. (2013). The results to be presented utilize a mesh density that is doubled in both directions with respect to that shown in Fig. 3. The boundary conditions for the creasing problem without the conducting channel are similar to those for the wrinkling problem aside from the multi-point constraints on the vertical displacement of the top surface. They are repeated here for clarity: the displacements and electric potential of the bottom surface of the domain are fixed to zero, the vertical sides of the domain are restricted from horizontal displacement, tangentially traction-free, and charge-free, the top surface is loaded electrically under charge-control by enforcing the uniform voltage using multi-point constraints, i.e. all of the electric potential degrees of freedom on the top surface are tied to the lead node located at $(0,h)$. Additionally, the top surface is traction-free except for the cases where a single nodal force F is applied to induce

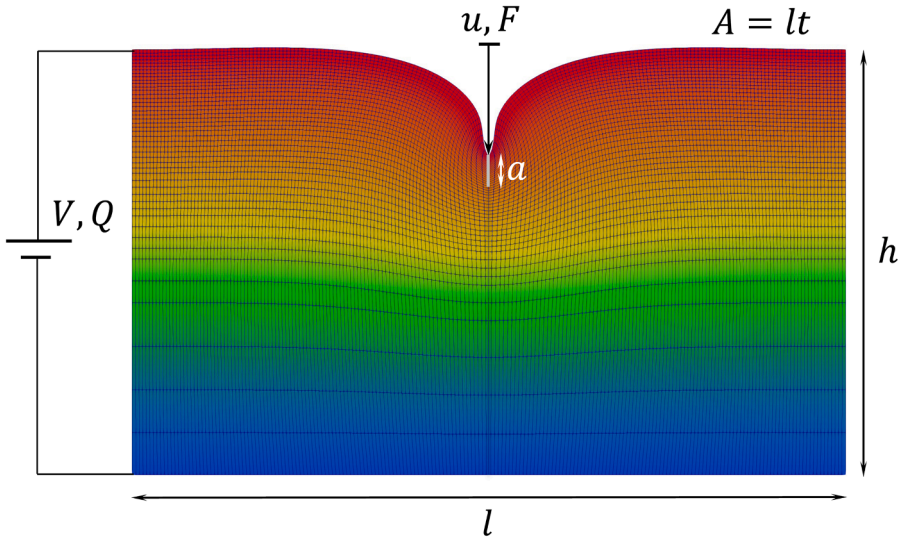

Fig. 3. Features of the creasing problem showing a result (color contours are for electric potential) with a lower mesh density (for viewing clarity) near the crease than what was used to report the results in Figs. 4-12. Those results utilize a mesh density that was doubled in both directions with respect to this figure. In addition to the parameters shown in Fig. 1, also shown are the nodal displacement and nodal force on the node at the crease tip, and a small non-opening conducting channel/crack of length a under the crease. This is the imperfection that is studied and argued to trigger creasing at voltage levels below the critical levels required for wrinkling. Note that the dimensions h and l are the film thickness and periodic domain size as measured with respect to the *pre-stretched* state and prior to the application of the voltage/charge.

the crease.

Fig. 4 shows the fundamental behaviors uncovered by these calculations for a film with $l/h = 2$, $\kappa/\mu = 1000$, and no pre-stretch ($\lambda_0 = 1$). Fig. 4a shows the downward displacement of the crease tip versus the applied charge and 4b shows the voltage versus charge response. Note that the critical voltage or charge for wrinkling is $\frac{V}{h}\sqrt{\frac{\varepsilon}{\mu}} = \frac{Q}{A\sqrt{\varepsilon\mu}} = \sqrt{2}$, as predicted by Eq. (2.23) for the incompressible limit. For these calculations the film has no imperfections and the stable equilibrium solution for the system is the flat state up to the critical wrinkling voltage, with a constant slope for the V-Q curve (nearly incompressible). Even with a small perturbing force F the film remains stable in the flat state until the critical voltage or charge. At the critical charge level, the surface instability can be triggered by the force, forming a localized crease at the stable equilibrium state. This equilibrium state is sufficiently removed from the flat state such that special methods must be used to compute it. We have found two methods. The first, which has been used by Park and co-workers, is to allow the system to evolve dynamically (Park et al., 2012 & 2013; Park and Nguyen, 2013). For this method we include inertial terms as well as viscous terms to damp the vibrations. Once the vibrations have settled then the inertial and viscous terms can be "turned off" and converged solutions for the creased state can be found. Here we note that the creased state as shown in Fig. 3 does not necessarily involve self-contact of the surface, as will be discussed in more detail later. In contrast, the creases formed by compression with no electric fields always involve contact (Hohlfeld, 2008; Hohlfeld and Mahadevan, 2011; Hong et al., 2009).

Once the system reaches the stable equilibrium branch of the creased state, the charge can be increased/decreased to probe the full extent of this branch. The upper solid blue branch of the displacement-charge response in Fig. 4a and the lower curved blue branch on the voltage-charge response in Fig. 4b constitute this stable creased branch. Upon exploring the lower limit for the charge on the creased branch we find another critical point at $Q/A \approx 1.16\sqrt{\varepsilon\mu}$ and $V/h \approx 1.14\sqrt{\mu/\varepsilon}$. Below this level of applied charge the only equilibrium state is the flat film. A third branch of interest residing between $1.16 < \frac{Q}{A\sqrt{\varepsilon\mu}} < \sqrt{2}$ is shown as the dotted red lines on Fig. 4a and b; This branch connects the two stable branches and represents an unstable equilibrium solution. The method for obtaining this branch also offers a second approach for locating the stable creased branch. The procedure is as follows. Apply charge to the flat film up to a value in the range $1.16 < \frac{Q}{A\sqrt{\varepsilon\mu}} < \sqrt{2}$. Hold the charge fixed at this level and then increase the downward displacement of the crease, u, while computing the force F required to maintain this node in position. The force-displacement responses for three such excursions are shown in Fig. 5, with the associated zero-force points, open circles for the unstable equilibria and filled circles for the stable equilibria, also indicated on Fig. 6a and b. Once a point on the stable branch is found, then this can be used to probe the remainder of the stable branch without any force applied. Note that the unstable branch is very close to the first stable branch for the flat state in the charge-voltage plane (Figs. 4b and 6b), because a small local deformation does not cause a significant change in the overall capacitance of the dielectric elastomer.

When considering the results in Fig. 5 we must recognize that the force F is not a concentrated point force, but rather a consistent nodal finite element force. Hence, it is more appropriate to regard it as a load distributed over the length of two elements, which for these calculations is $2h_E = h/100$. Given this caveat, it is interesting to note that the flat state is stable against small perturbations at the charge/voltage levels shown in Fig. 5 and there is a finite barrier that must be overcome to evolve to the equilibrium creased state. It will be shown that conducting defects are effective at overcoming this barrier between the flat and creased states. The magnitude of

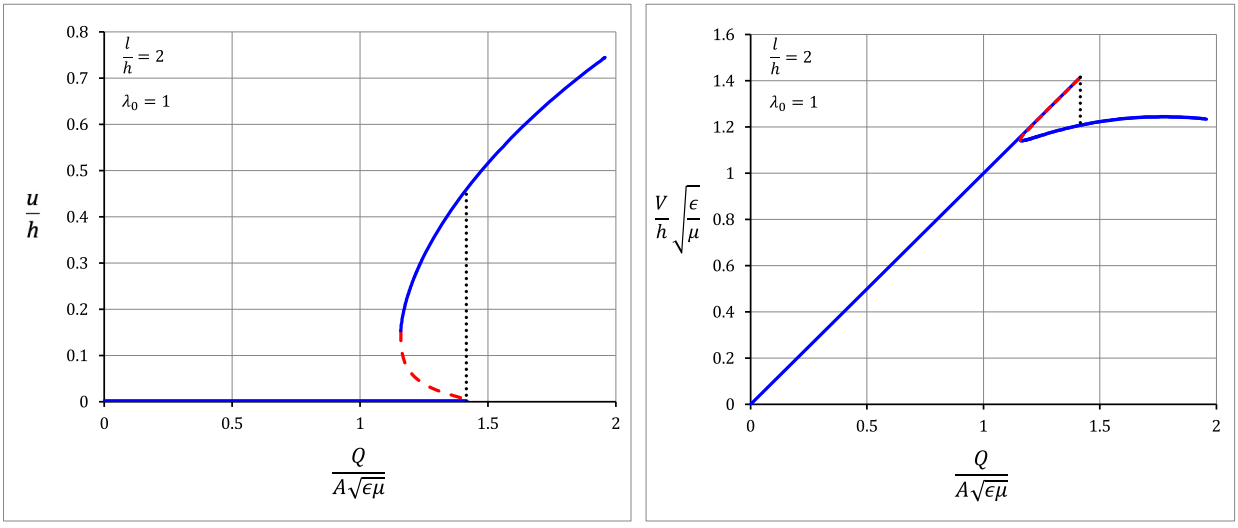

Fig. 4. Fundamental behaviors of creasing by the finite element calculations for a dielectric elastomer film with $l/h = 2$, $\kappa/\mu = 1000$, and no pre-stretch ($\lambda_0 = 1$). (a) The downward displacement of the crease versus the applied charge. (b) The applied voltage versus the charge. The solid blue lines are stable equilibrium solutions. The dashed red lines are unstable equilibrium solutions. The dotted black line is an unstable non-equilibrium path at fixed charge between the flat equilibrium state and the creased state at the critical voltage of $V/h = \sqrt{2\mu/\varepsilon}$.

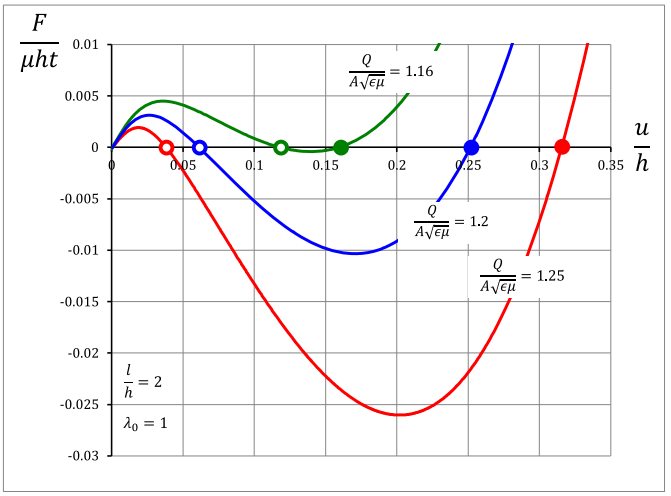

Fig. 5. The consistent nodal force F versus the induced crease tip displacement u of a perfectly flat film with no pre-stretch at three levels of applied charge. The dots indicate the zero-force solutions with the open circles on the unstable branch, and the filled circles on the stable branch, also marked on Fig. 6.

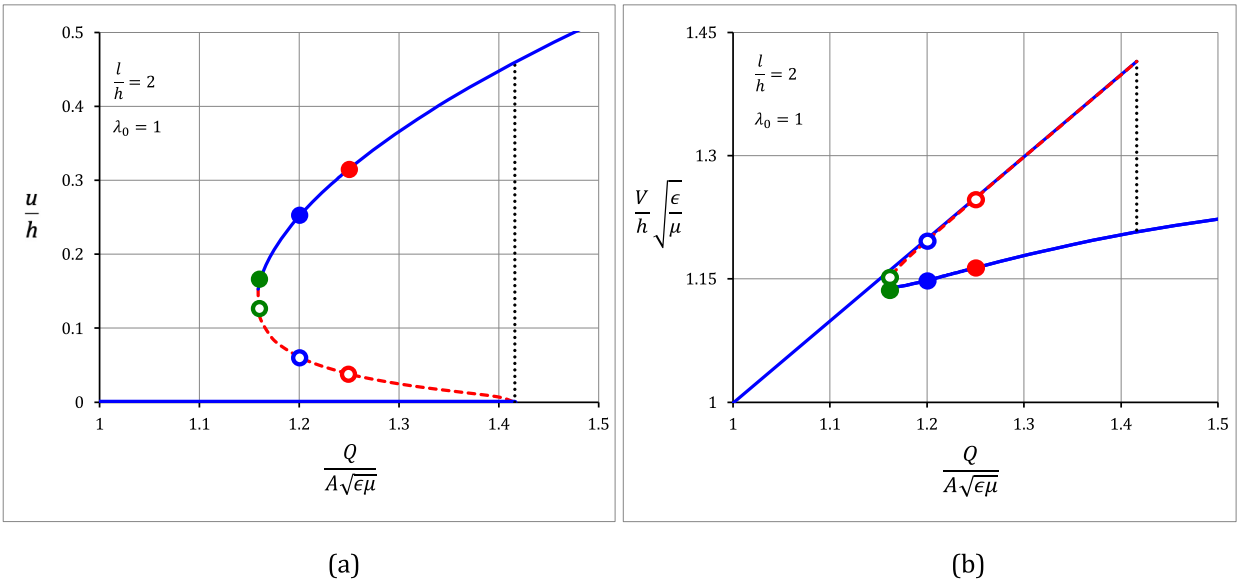

Fig. 6. A detailed view of Fig. 4a and b, with the stable (filled circles) and unstable (open circles) equilibrium points corresponding to those shown on Fig. 5.

this barrier decreases as the applied charge increases. At the critical charge for wrinkling, $Q/A = \sqrt{2\epsilon\mu}$, the barrier disappears, as the slope of the force-displacement curve becomes zero at $u = 0$. However, the calculation diverges before reaching the equilibrium creased state at the critical charge level, because of severely distorted elements at the crease tip. Nevertheless, the stability of the flat state (against small perturbations) is determined by the initial slope of the force-displacement curve. Moreover, by integrating the force-displacement curve in Fig. 5, we can calculate the energy difference between the flat state and the creased state. Evidently, the stable equilibrium creased state has a higher energy at $Q/A = 1.16\sqrt{\varepsilon\mu}$, but has a lower energy at $Q/A = 1.2\sqrt{\varepsilon\mu}$ (see Fig. 5). At a charge level slightly above $Q/A = 1.16\sqrt{\varepsilon\mu}$, the two stable equilibrium states have the same energy. Denote this charge level as Q_M. Then, for $Q_M/A < Q/A < \sqrt{2\,\varepsilon\,\mu}$, the equilibrium creased state has a lower energy than the flat state. Thus, while both the flat and creased states are stable against small perturbations in the range $Q_M/A < Q/A < \sqrt{2\,\varepsilon\,\mu}$, the creased state is the global energy minimum. It is found that Q_M/A is slightly larger than $1.16\sqrt{\varepsilon\mu}$ in this calculation with $l/h = 2$ but approaches a value of $1.14\sqrt{\varepsilon\mu}$ when the computational domain size l/h increases (see Fig. 10).

It must be disclosed that there are no contact constraints enforced in any of the calculations in this work and interpenetration of the

creased surface is numerically allowed and does occur in several regimes of the electromechanical loading. For example, for the present case under discussion here, while there is no interpenetration or contact at the critical creasing charge $Q/A = 1.16\sqrt{\varepsilon\mu}$, self-contact does occur if the electrical loading is increased to a charge level of $Q/A = 1.196\sqrt{\varepsilon\mu}$, and the contact area increases further with additional electrical loading. Fig. 7a shows the deformed shape of the crease at the critical charge $Q/A = 1.16\sqrt{\varepsilon\mu}$, and Fig. 7b shows the state where self-contact first occurs at $Q/A = 1.196\sqrt{\varepsilon\mu}$. For $Q/A = 1.196\sqrt{\varepsilon\mu}$, interpenetration occurs in the crease and thus the crease solution is no longer physically meaningful. Nevertheless, the critical condition for the onset of the creasing instability can be determined from these calculations.

Another observation of note from Fig. 7 is that upon formation, the crease extends to a finite depth of approximately $0.13h$ for the case shown. This is in apparent contrast to the mechanically induced creasing problem where it is accepted that there is no length scale controlling the crease depth (Hohlfeld, 2008; Hohlfeld and Mahadevan, 2011; Hong et al., 2009). For the electromechanical problem here, the formation of a crease creates a concentration of charge along the crease tip. This acts like a line of charge that is attracted to the bottom electrode at the depth h. Thereafter the crease deepens to minimize the combination of elastic and electrical energy in the film. In this problem the film thickness plays a critical role as a length scale in the post-bifurcation behavior.

We now identify two critical voltages of interest. The maximum voltage where the flat state is stable (against small perturbations) is called the wrinkling voltage, V_W, since this corresponds to the analytical result for the onset of wrinkling discussed in Section 2, and the minimum threshold voltage where the creased state is stable is called the creasing voltage, V_C. For the case with no pre-stretch discussed above, $V_W/h = \sqrt{2\mu/\varepsilon}$ and $V_C/h = 1.14\sqrt{\mu/\varepsilon}$ (see Fig. 6a). For $V < V_C$, the flat state is the only equilibrium state and is thus stable against all perturbations (small or large). For $V_c < V < V_W$, the flat state is stable against small perturbations, but nucleation of creases is possible with a barrier that may be overcome due to the presence of surface defects. For $V \geq V_W$, the flat state becomes unstable against small perturbations, and nucleation of creases can occur with no barrier. Therefore, the two critical voltages, V_W and V_C, set the upper and lower theoretical bounds for the critical voltages in experiments where surface defects are commonly expected. Theoretically, it is possible to determine another critical voltage V_M between the two bounds, for which the flat state and the equilibrium creased state have the same energy. This corresponds to a Maxwell condition at which a crease can extend with no change in voltage. Then, for $V_C < V < V_M$, the creased state has a higher energy than the flat state; for $V_M < V < V_W$, the creased state has a lower energy than the flat state, so that the creased state is the stable state with the global minimum energy whereas the flat state is metastable. It is found, that V_M/h is slightly larger than $1.14\sqrt{\mu/\varepsilon}$ in this calculation with $l/h = 2$ but approaches $1.14\sqrt{\varepsilon\mu}$ when the computational domain size l/h increases (see Fig. 10).

Next we discuss the effects of pre-stretch on the critical voltages. Fig. 8 shows the two critical voltages for a range of equi-biaxial pre-stretch, $0.666 < \lambda_0 < 3$. First note that the critical wrinkling voltage from the finite element simulations with $\kappa/\mu = 1000$ is practically identical to the analytic solution given in Eq. (1.1) for an incompressible neo-Hookean material. Additionally, the critical voltage for wrinkling drops to zero at an equi-biaxial stretch level of $\lambda_0 = 0.666$, which is the critical equi-biaxial stretch for compression induced surface wrinkling first derived by Biot (1963). In contrast, the critical voltage for creasing drops to zero at an equi-biaxial stretch level of $\lambda_0 = 0.736$, which is nearly identical to the critical equi-biaxial stretch for compression induced creasing obtained previously (Hohlfeld and Mahadevan, 2008 and 2011; Hong et al., 2009). Again, self-contact was not prohibited in the creasing calculations and interpenetration of surfaces does occur in a range of loading cases. The absence of contact constraints does not affect the critical voltage for creasing since the initial transition to creasing does not involve self-contact. However, after a finite level of creasing develops, self-contact can occur, as shown in Fig. 7b. On Fig. 8, self-contact occurs for the finite crease at the critical creasing voltage for equi-biaxial pre-stretches in the range of $0.736 < \lambda_0 < 0.9$. For $\lambda_0 > 0.9$ self-contact does not occur at the critical creasing voltage, but it may occur upon increased electrical loading to higher voltages. Furthermore, the critical creasing behavior can also be separated by the character of the transition from the flat state to the creased state at the critical voltage V_C. Here we identify a discontinuous transition, which is characterized by a jump in the crease displacement at V_C (see Figs. 4 and 6), versus a continuous transition, which is characterized by no jump in the crease displacement at V_C (see Fig. 9). The finite element calculations establish the change from the discontinuous to continuous transition at an equi-biaxial stretch level of $\lambda_0 \approx 2.4$. However, note that the wrinkling

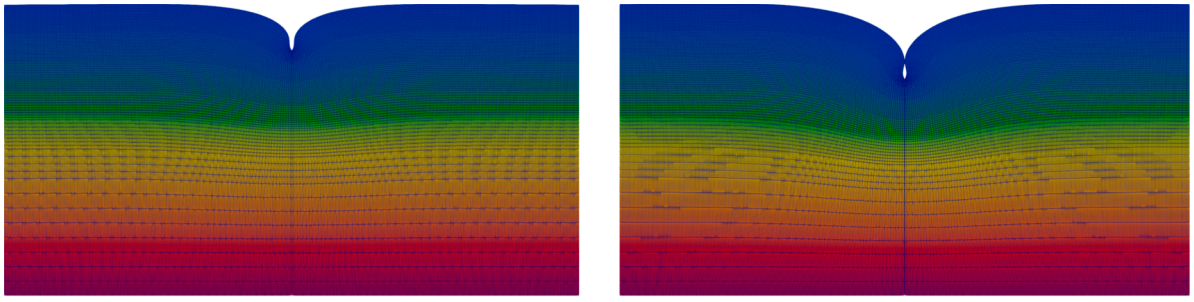

Fig. 7. The deformed shapes of the crease for the film with no pre-stretch, $\lambda_0 = 1$, as reported in Figs. 4 and 6: (a) at the critical charge for creasing $Q/A = 1.16\sqrt{\varepsilon\mu}$, and (b) at the charge level $Q/A = 1.196\sqrt{\varepsilon\mu}$ when self-contact first occurs in the crease. The color contours represent the electric potential.

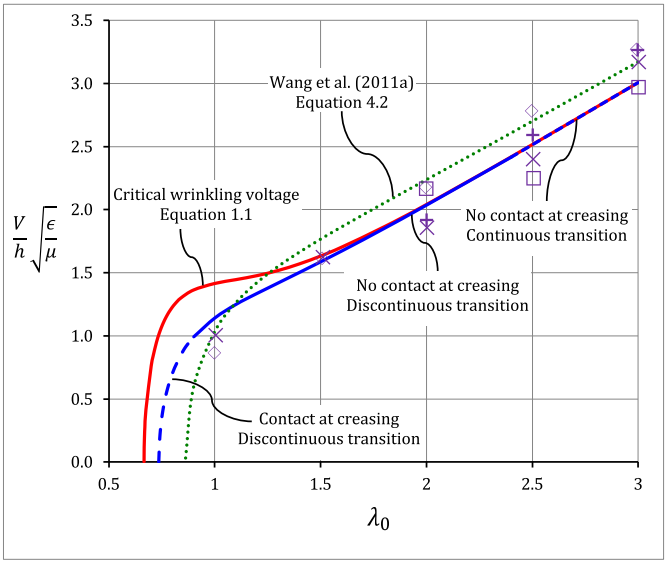

Fig. 8. The critical voltages for wrinkling (red curve), creasing (blue curve), Eq. (4.2) (green dotted line) and experimental measurements (purple markers) from Wang et al. (2011a). The curve for the creasing voltage is divided into three regions. For $0.736 < \lambda_0 < 0.9$ the transition to creasing results in self-contact. This region also has a jump in the transition from the flat to the creased state, similar to the behavior shown in Figs. 4 and 6. For $0.9 < \lambda_0 < 2.4$ the initial transition to creasing does not result in self-contact, but the transition to creasing is discontinuous. Finally, for $\lambda_0 > 2.4$ the transition does not result in self-contact and is continuous with behavior similar to that shown in Fig. 9.

voltage V_W and the creasing voltage V_C are nearly indistinguishable for a biaxial stretch level of $\lambda_0 > 2$ in Fig. 8.

We compare the critical voltages to the experiments by Wang et al. (2011a), also shown as the purple markers in Fig. 8. The measured critical voltages for the creasing instability in Ecoflex (a silicone elastomer) films increased with increasing pre-stretch, similar to the critical creasing voltage (V_C) in Fig. 8. For the case of no pre-stretch ($\lambda_0 = 1$), the critical voltage was measured to be around $V_C/h \approx 1.03\sqrt{\mu/\varepsilon}$, which is slightly lower than the numerical result of $1.14\sqrt{\mu/\varepsilon}$ (by ~10%). With an equi-biaxial pre-stretch ($\lambda_0 > 1$), the data was more scattered, with an average value of $V_C/h \sim 2\sqrt{\mu/\in}V_C/h \sim 2\sqrt{\mu/\varepsilon}$ for $\lambda_0 = 2$ and $\sim 3\sqrt{\mu/\in}\sim 3\sqrt{\mu/\varepsilon}$ for $\lambda_0 = 3$, both in close agreement with the numerical results in Fig. 8 for V_C. A theoretical model was also presented by Wang et al. (2011a), which predicted the critical voltage as

$$\frac{V_C}{h} = \sqrt{\frac{\mu}{\varepsilon}\left(1.06 + \lambda_0^2 - \lambda_0^{-4}\right)} \tag{4.2}$$

where the value of 1.06 was obtained by fitting to the experiments for the case of no pre-stretch ($\lambda_0 = 1$). As shown in Fig. 8, Eq. (4.2) is fairly close to the numerical result for $\lambda_0 > 1$, but it under-predicts the critical voltage for $\lambda_0 < 1$. In particular, Eq. (4.2) predicts a zero critical voltage for $\lambda_0 = 0.863$, considerably larger than the critical equi-biaxial stretch for compression induced creasing (Hohlfeld and Mahadevan, 2008 and 2011; Hong et al., 2009). In addition, Wang et al. (2011a) calculated the critical electric field for the creasing instability, following the method by Hong et al. (2009). However, their numerical results appear to have considerably overestimated the critical voltage, as noted by Hutchinson (2021). One possible cause may be their assumption of self-contact in calculating the potential energy of the creased state, which is not the case for $\lambda_0 > 0.9$ at the critical voltage.

Fig. 9 shows the continuous transition from the flat state to a periodically groove-like (shallow, smooth-bottomed, and localized) undulated surface for the case with an equi-biaxial pre-stretch $\lambda_0 = 3$ and with periodic domain sizes of $l/h = 2$ and $l/h = 28$. Unlike the discontinuous transition shown in Fig. 4 for $\lambda_0 = 1$, the voltage and undulation displacement increases continuously with the applied charge near the bifurcation, similar to the classical buckling of elastic plates under compression. The critical voltage, $V_C/h = 3\sqrt{\mu/\varepsilon}$, is nearly identical to that predicted for onset of wrinkling by Eq. (1.1), independent of the domain size. Thus, the onset of bifurcation with the continuous transition can be well predicted by the linear perturbation analysis as detailed in Hutchinson (2021) and Hutchinson et al. (2022). Beyond the critical electrical load, the flat state is unstable and surface undulations develop with no barrier. The post-bifurcation behavior involves nonlinear interactions among simultaneously unstable wrinkle modes of short wavelengths, forming a downward groove-like undulation (Fig. 9c and d). In contrast, the onset of bifurcation with a discontinuous transition (Fig. 4) has a critical voltage lower than that for onset of wrinkling, and there exists an energy barrier between the flat state and the creased state with a highly localized deformation. Therefore, with increasing pre-stretch, the bifurcation mode transitions from discontinuous creasing-like ($\lambda_0 < 2.4$) to continuous groove-like ($\lambda_0 > 2.4$). A similar creasing-wrinkling transition was observed previously in elastomer films under electric fields by varying the ratio between surface energy and shear modulus of the elastomer (Wang and Zhao, 2013).

Fig. 9c, for $\lambda_0 = 3$, raises the issue of the effect of the periodic domain size l/h. First note that the depth of the groove increases

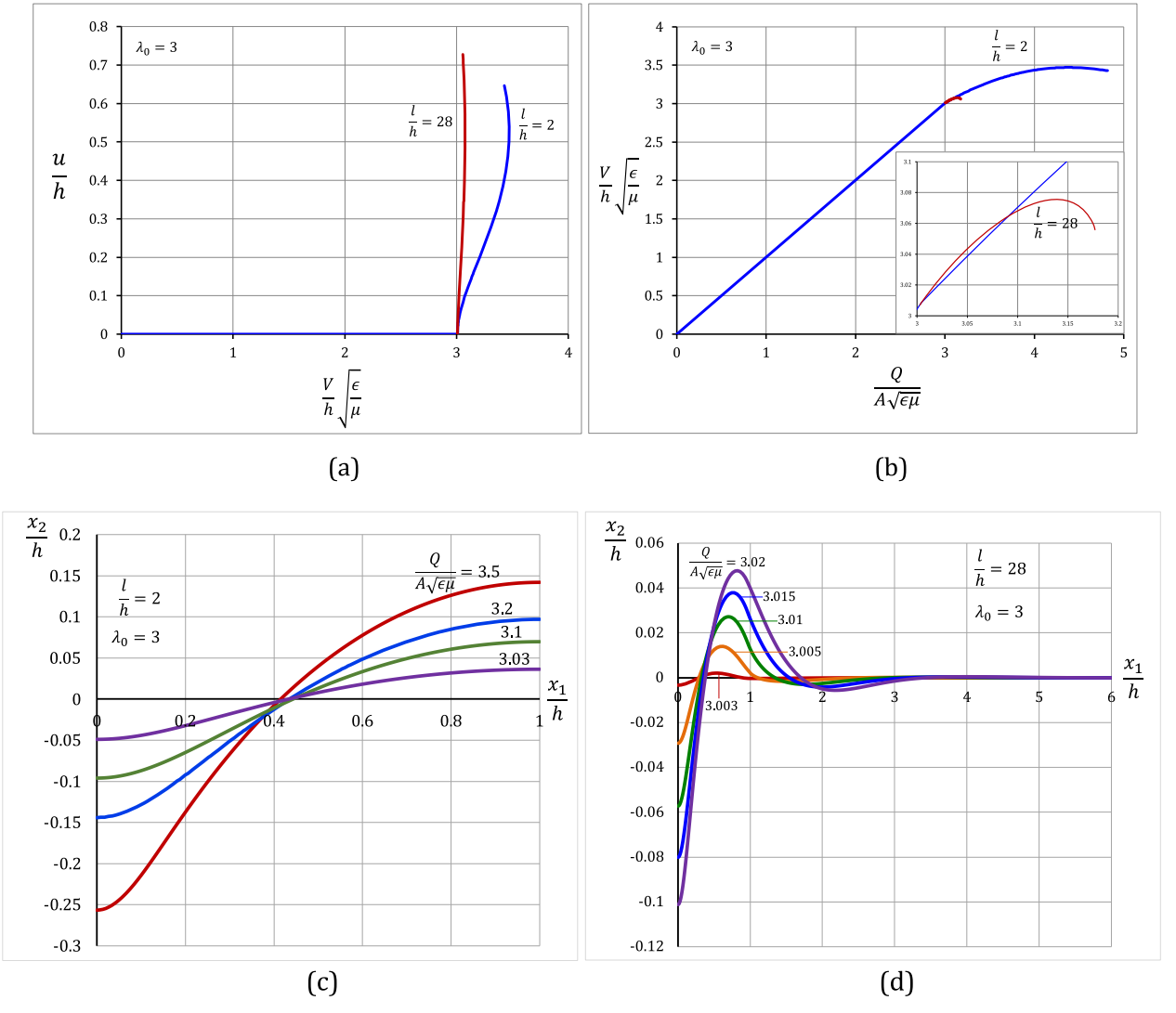

Fig. 9. The groove-like response for $l/h = 2$ and $l/h = 28$. (a) The groove-like surface displacement-voltage behavior, (b) the voltage-charge behavior, and (c) and (d) deformed surface shapes at multiple charge levels for the dielectric elastomer film with an equi-biaxial pre-stretch $\lambda_0 = 3$. The critical voltage for creasing for this case is, $V_C/h = 3\sqrt{\mu/\varepsilon}$. A continuous transition is observed, in contrast to the discontinuous shown in Fig. 4 for $\lambda_0 = 1$. The case with $l/h = 2$ is not long enough to allow the localized groove geometry to fully develop without interacting with a neighboring groove.

continuously from zero starting at the critical voltage/charge, $\frac{V_C}{h}\sqrt{\frac{\varepsilon}{\mu}} = \frac{Q_C}{A\sqrt{\varepsilon\mu}} = 3$. Furthermore, the shape of the deformed surface is *not* of the functional form of that found in the analytical wrinkling analysis, i.e. $u_2 \sim \cos x_1$ and $u_1 \sim \sin x_1$. A shape such as this can form as a superposition of the multiple simultaneous sinusoidal eigenmodes associated with the critical wrinkling voltage in the short wavelength limit, as shown by Hutchinson (2021). However, the deformed surface shape clearly does not appear as localized as in the creasing case with $\lambda_0 = 1$ (see Fig. 7). These observations motivated the need to study the effects of the periodic domain size l/h. Fig. 9d shows the deformed surface shape for the case with $\lambda_0 = 3$ and $l/h = 28$. The more localized groove-like deformation pattern of the surface now becomes evident. Additionally, to the precision that can be expected from the finite element calculations, the critical voltage for bifurcation does not change for $l/h = 28$ from that for $l/h = 2$. This feature of the critical voltage was verified over the entire range of pre-stretch that was studied. While the critical voltage for bifurcation is unaffected by the periodic domain size, the post-bifurcation response is clearly altered. Further discussion of the localized mode form above the discontinuous/continuous transition is presented in the Conclusions.

The effects of the periodic domain size on the post-bifurcation responses are further illustrated in Figs. 10 and 11 for the case with no pre-stretch, $\lambda_0 = 1$. Fig. 10 are the analogous plots to Fig. 6 and include the same curves for $l/h = 2$. However, the abscissa for Fig. 10a has been changed to the normalized voltage as opposed to the normalized charge. These two plots illustrate features that are common to post-bifurcation behaviors.

Fig. 10a includes data from Fig. 6a for $l/h = 2$, but now plotted as the normalized depth of the crease, u/h, as a function of the normalized voltage. Results computed for $l/h = 8$ and $l/h = 28$ plot on top of those for $l/h = 2$ because the localized crease geometry is not altered by increasing the length of the computational region assuming is not less than about $l/h = 2$[1]. On the other hand, the behavior seen in Fig. 10b for larger l/h reflects the fact that the vertical component of the electric displacement over almost all the layer is linearly related to the applied voltage as $D_2 = -\varepsilon V/h$ except in the region of localized deformation where the electric displacement becomes highly concentrated. As creasing proceeds, most of the additional charge added to the surface migrates to the localized crease. Thus, the solution branch as plotted becomes closer and closer to the linear uniform solution as l/h becomes large. For this plot, the limit for $l/h \to \infty$ would lie on top of the result for the uniform layer, as seen in the trend in Fig. 10b, with a lower bound at $\frac{V_C}{h}\sqrt{\frac{\varepsilon}{\mu}} = \frac{Q_C}{A\sqrt{\varepsilon\mu}} = 1.14$ as the critical condition for creasing. This behavior is akin to necking in bars and to the post-buckling behavior of thin-walled tubes where the additional post-bifurcation deflection is localized to the neck or buckle as longer and longer geometries are considered.

Fig. 10a illustrates that the post-bifurcation crease deflection versus the applied voltage is largely independent of the periodic domain size for $l/h \geq 2$. Additionally, Fig. 11 shows the deformed surface profiles for the creased state at the critical applied voltage of $V_C/h = 1.14\sqrt{\mu/\varepsilon}$ for $\lambda_0 = 1$. Here it is evident that for $\lambda_0 = 1$ the crease is highly localized and deep as opposed to $\lambda_0 = 3$ in Fig. 9 where the groove-like profile is shallower and more extended. Most importantly, the shape of the crease in Fig. 11 is relatively insensitive to l/h, fully confirming the localized nature of the crease solution for $\lambda_0 = 1$.

The final set of simulations to be presented concern the introduction of a small conducting, mechanically closed, channel of length a to trigger the transition to creasing near the critical voltage V_C. Recall that for the cases with a discontinuous transition, there is a finite barrier between the flat state and the equilibrium creased state at V_C, and so the flat state is stable against small force perturbations (see Fig. 5). We also studied the effects of small but smooth localized perturbations of the meshed geometry and the story is the same, the flat state is stable against small perturbations up to the critical voltage for wrinkling V_W. It is hypothesized that small conducting defects as shown in Fig. 3 (a vertical segment of length a located at $x_1 = 0$ and penetrating into the elastomer layer), may act to trigger the transition from the flat to the creased state at the lower critical voltage V_C. In this work two defect sizes were studied, one with $a/h = 1/120$ (green curves in Fig. 12) and a second with $a/h = 1/48$ (crimson curves in Fig. 12). Note that these defects were not resolved with a fine mesh but rather implemented within the same mesh used to study the perfectly flat film. The shorter channel is only two elements deep and the longer is 5 elements deep. The goal here was to introduce a physically motivated defect geometry with an intensity that increases as the electrical loading is increased. Strictly speaking such defects introduce electrical "crack"-like singularities into the structure, but we have made no effort to resolve or characterize this singularity. Hence, these results should be interpreted with these caveats in mind.

Fig. 12 illustrates the effect of the conducting channel on the displacement-charge and voltage-charge response of a nearly incompressible dielectric elastomer film with no pre-stretch ($\lambda_0 = 1$) and a periodic domain size of $l/h = 2$. The primary feature of these results is that the flat state is no longer stable at the critical creasing voltage V_C. In fact, the downward deflection of the channel begins as soon as any voltage is applied to the film. However, significant displacements of the crease and deviations from the linear voltage-charge response only become evident near V_C. It is of note that the behaviors for the longer channel show a smooth transition from the nearly flat to the creased state, while the shorter channel still shows a discontinuous transition near V_C. However, in contrast to the case with no defect, where the flat state is stable at V_C, the case with the small-channel defect is unstable at a voltage of approximately $V/h = 1.14\sqrt{\mu/\varepsilon}$. We suspect that it is this type of conducting surface defect that acts to trigger the creasing instability at electrical loading levels of $V/h \approx \sqrt{\mu/\varepsilon}$ for $\lambda_0 = 1$ in experiments (Wang et al., 2011a, 2011b), which are significantly lower than the critical voltage for wrinkling instability, $V/h = \sqrt{2\mu/\varepsilon}$.

[1] For small l/h the crease deformation is influenced by the periodic boundary conditions. Consequently, the displacement/voltage behavior is somewhat different, and the critical voltage for creasing is larger than that shown in Figure 10 but remains below the critical voltage for wrinkling. For example, when l/h=0.5 the critical voltage for creasing is V_c/h=1.246$\sqrt{(\mu/\varepsilon)}$.

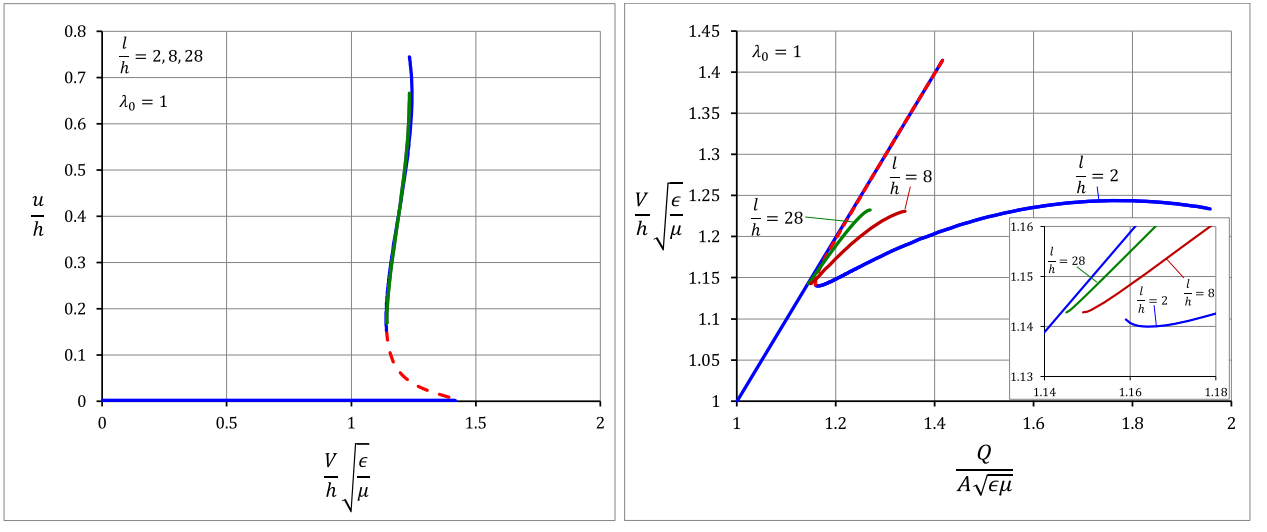

Fig. 10. (a) The crease deflection versus the applied voltage for three different periodic domain lengths and no pre-stretch, $\lambda_0 = 1$. All three cases collapse onto one another. (b) The voltage versus charge response for the same cases.

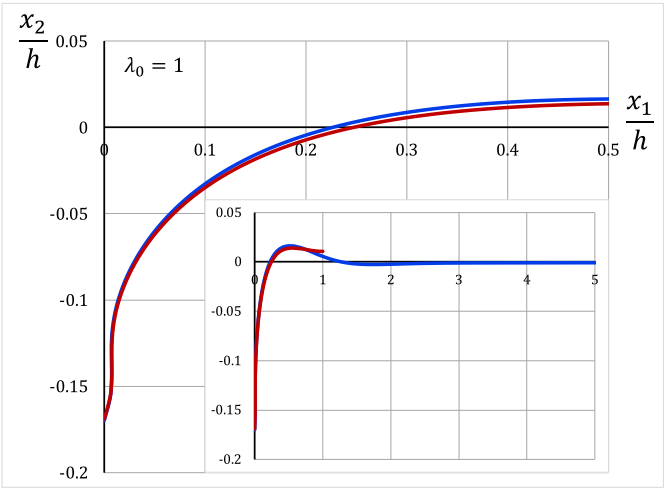

Fig. 11. Deformed surface shape (half-crease) for two different periodic domain lengths, $l/h = 2$ (red) and $l/h = 28$ (blue), with no pre-stretch, $\lambda_0 = 1$, at the critical creasing voltage of $V_C/h = 1.14\sqrt{\mu/\varepsilon}$. The larger plot is focused near the crease, and the inset is a wider view-frame.

5. Conclusions

Fig. 8 presents a consistent theoretical picture of the juxtaposition of wrinkling and creasing instabilities in a nearly incompressible dielectric elastomer layer that is first subject to equi-biaxial pre-stretch, bonded to a rigid substrate, and then subject to a voltage difference imposed across the layer's upper and lower conducting surfaces. The results in this paper were computed using a compressible elastic solid whose incompressible limit is neo-Hookean. The results in Fig. 8 were computed with a ratio of bulk to shear modulus given by $\kappa/\mu = 1000$ corresponding to a Poisson's ratio, $\nu = 0.4995$ and, therefore, essentially the incompressible limit. With no imposed voltage, the Biot wrinkling instability occurs at an equi-biaxial pre-compression of $\lambda_0 = 0.666$ while the threshold for the creasing instability is at the smaller pre-compression, $\lambda_0 = 0.736$. With no pre-stretch, $\lambda_0 = 1$, the critical voltage for the wrinkling instability is $V_W/h = \sqrt{2\mu/\varepsilon}$ while the critical voltage for creasing is about 20% lower at $V_C/h = 1.14\sqrt{\mu/\varepsilon}$. The voltage at the onset of wrinkling for the neo-Hookean solid increases with pre-stretch as given by Eq. (1.1). As the pre-stretch increases, the difference between the critical voltages at the onset of wrinkling and the creasing threshold diminishes and, according to the numerical simulations carried out in this paper, becomes zero for λ_0 greater than about 2.4. The transition from the flat state to the creased state is discontinuous for $\lambda_0 < 2.4$ but becomes continuous for $\lambda_0 > 2.4$. In the range of $0.736 \le \lambda_0 \le 0.9$, the crease solutions have self-contact, but for $\lambda_0 > 0.9$ the threshold crease solutions are open, i.e., do not have self-contact, although at some voltage above threshold self-contact will generally occur. At pre-stretches above $\lambda_0 = 2.4$, the bifurcation mode that emerges in our simulations is localized (c.f., the discussion related to Fig. 9) and in the shape of a groove-like entity.

In most respects the theoretical picture in Fig. 8 aligns nicely with the experimental data of Wang et al. (2011a) for silicone elastomer layers subject to equi-biaxial pre-stretch in the range $1 \le \lambda_0 \le 3$. Critical voltages corresponding to the occurrence of crease-like modes were measured for multiple layers (typically 4) at each of the following pre-stretches: $\lambda_0 = 1,\ 1.5,\ 2,\ 2.5,\ \&\ 3$. The scatter of the measured voltage ranged from about 10 to 20% at each pre-stretch level. As discussed in the body of the paper, the mean value of the measured voltage is reasonably close to the predicted crease threshold in Fig. 8. The scatter is consistent with the strong imperfection-sensitivity expected for creasing and localization, and no doubt in some part due to difficulties in conducting the experiments. One possible inconsistency between the present theoretical findings and the experimental data is that the greatest scatter (about 20%) occurs for layers with pre-stretch $\lambda_0 = 2.5$ for which a continuous transition is predicted by the present simulations and is not expected to be imperfection sensitive. Indeed, the scatter of the experimental data for $\lambda_0 = 3$ is only about 10%. Moreover, the difference between highly localized creases and groove-like deformation predicted by the present simulations has not been observed.

The initial post-bifurcation Koiter analysis carried out by Hutchinson et al. (2022) (see also the supplementary materials of that work) also predicted decreasing imperfection-sensitivity and decreasing intensity of the instability with increasing equi-biaxial pre-stretch, but it does not predict the definitive transition to continuous initial post-bifurcation behavior that emerges in the simulations in this paper for $\lambda_0 > 2.4$. This may reflect a limitation (or possibly an error) in the initial post-bifurcation analysis. The initial post-bifurcation analysis considers only the terms in the perturbation expansion of next higher order beyond those determining the wrinkling condition, and it is possible that the neglected higher-order terms may be important. Another interesting feature of the mode that is predicted for pre-stretches above the discontinuous/continuous transition is that it appears to be immediately localized. We are unaware of any other example where a stable bifurcation gives rise to a localized bifurcation mode, although superposition of the multiple sinusoidal modes could make this possible. These are open issues worthy of further exploration.

A clear transition between creasing and wrinkling has been exhibited by another set of experiments on constrained elastomeric layers conducted by Wang and Zhao (2013). As noted in Hutchinson (2021), surface energy, γ, places a lower limit on the size of wrinkles or creases with the relevant dimensionless parameter being $\gamma/\mu h$. The experiments of Wang and Zhao (2013) involved

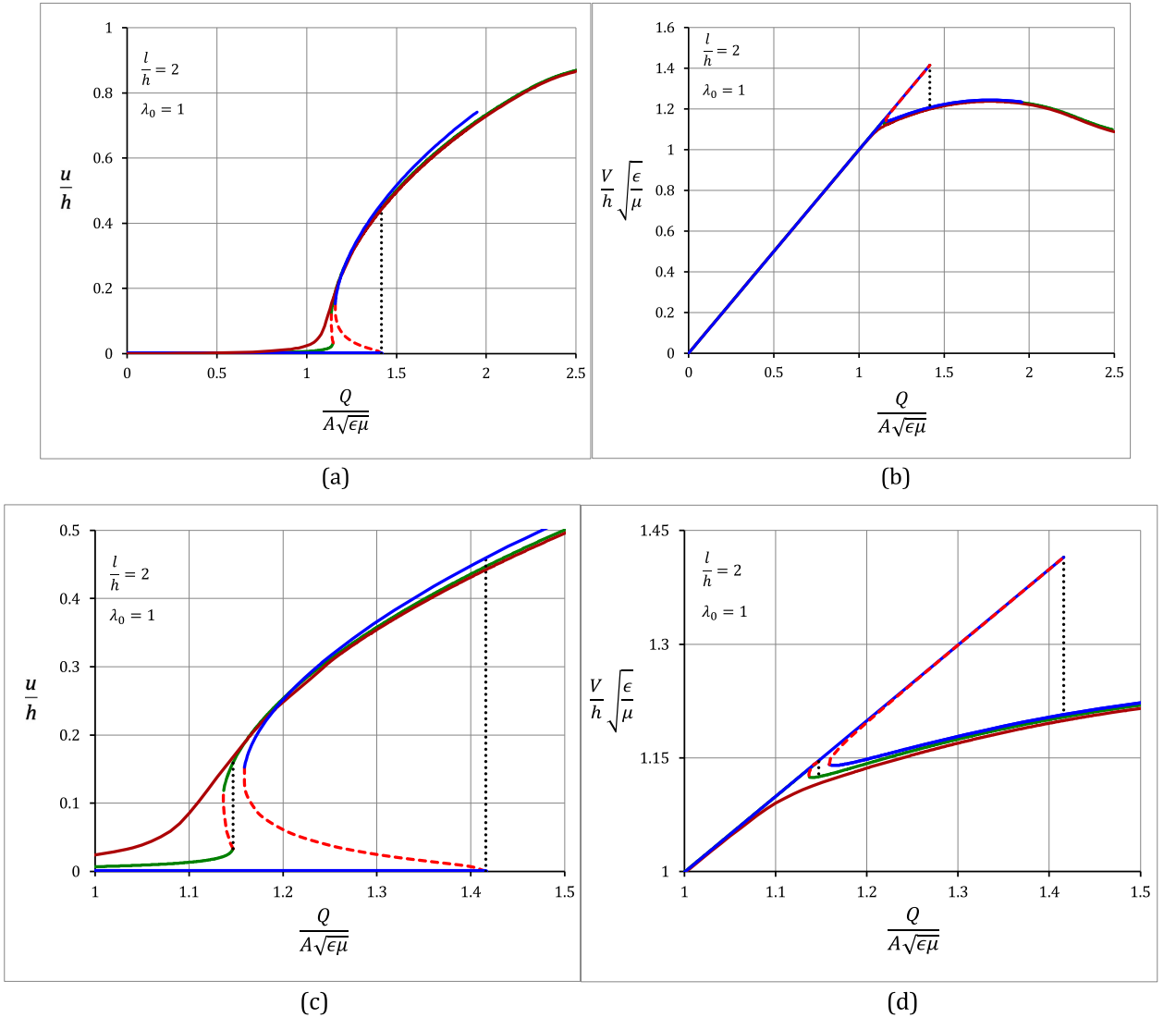

Fig. 12. (a,c) Crease displacement-charge, and (b,d) voltage-charge behaviors for the dielectric elastomer film with no pre-stretch ($\lambda_0 = 1$) and a small conducting defect. The green curves (with red dashed unstable branch) are for a conducting channel depth of $a/h = 1/120$ and the crimson curves are for a depth of $a/h = 1/48$. The results of Figs. 4 and 6 are repeated here for comparison.

measuring the critical voltage and observing the mode shapes for a sequence of layers with increasing $\gamma/\mu h$. For sufficiently small $\gamma/\mu h$ creasing was observed, but above values of $\gamma/\mu h$ on the order of unity wrinkles were observed. By including surface energy, we believe the approach introduced in this paper should be able to accurately characterize this transition and the behavior associated with it.

Finally, it seems worthwhile to call attention to another application of current interest where stable localized solutions exist at loads below the critical bifurcation condition. Starting with the work of Horak et al. (2006), , and continued by Kreilos and Schneider (2017). Formation of surface wrinkles and creases in constrained dielectric elastomers subject to electromechanical loading and Groh and Pirrera (2019), stable localized buckling solutions of axially compressed elastic cylindrical shells have been identified which exist at loads roughly 50% below the bifurcation load of the perfect shell. As in the present paper, the numerical methods employed by the authors of these papers permit the delineation of the evolution of the localized modes along the stable branches of the solutions. Like the phenomenon investigated here, where for the discontinuous bifurcation the crease depth at the critical voltage V_c scales with the layer thickness, the localized shell buckles also have a well-defined size determined by the thickness to radius ratio of the shell.

Declaration of Competing Interest

The authors declare that they have no known competing financial interests or personal relationships that could have appeared to influence the work reported in this paper.

Acknowledgments

The authors acknowledge helpful discussions with Prof. Stelios Kyriakides of the University of Texas at Austin on analogous instability and localization phenomena such as necking and shell buckling. CML acknowledges the help from Jash Pujara on some of the initial numerical investigations.

Appendix A. Additional details of the Q1P0 Element Formulation

For the 4-noded Q1P0 element, the electric potential and displacement fields are interpolated from the associated nodal values, ϕ^M and u_i^M, using standard bilinear shape functions, N^M, where the superscript M ranges from 1 to 4 and summation is assumed over the repeated superscripts in the formulae below, and as shown $B_i^M = \partial N^M/\partial X_I$.

$$\phi = N^M\phi^M \rightarrow E_I = N^M_{,I}\phi^M = B^M_I\phi^M \tag{A.1}$$

$$u_i = N^M u_i^M \rightarrow F_{iJ} = B^M_J u_i^M \rightarrow \overline{F}_{iJ} = \widetilde{B}^M_{iJk}u_k^M \tag{A.2}$$

Note that the B_i^M are independent of the deformation, but the $\widetilde{B}^M_{iJk}$ are dependent on the deformation and given as follows,

$$\widetilde{B}^N_{iJk} = \theta^{\frac{1}{3}}J^{-\frac{1}{3}}\left(\delta_{ik}B^N_J + \frac{1}{3}\theta^{-1}F_{iJ}\widehat{B}^N_k - \frac{1}{3}F^{-1}_{Lk}F_{iJ}B^N_L\right) \tag{A.3}$$

where,

$$\widehat{B}^N_i = \frac{1}{V_E}\int_{V_E} JF^{-1}_{Ji}B^N_J dV_0 \tag{A.4}$$

Here, V_E represents the volume of the element. Furthermore, for the derivation of the tangent stiffness, the variations of $\widetilde{B}^N_{iJr}$ with respect to the nodal displacements u_s^M are required and given as,

$$\begin{aligned}\widetilde{dB}^{NM}_{iJrs} = {}& \frac{1}{3}\theta^{\frac{1}{3}}J^{-\frac{1}{3}}\Bigg[-\frac{2}{3}\theta^{-2}F_{iJ}\widehat{B}^N_r\widehat{B}^M_s - \frac{1}{3}\theta^{-1}F_{iJ}\left(\widehat{B}^N_r F^{-1}_{Qs}B^M_Q + \widehat{B}^M_s F^{-1}_{Qr}B^N_Q\right) + \\ & \theta^{-1}\delta_{is}\widehat{B}^N_r B^M_J + \theta^{-1}\delta_{ir}\widehat{B}^M_s B^N_J + \frac{1}{3}F_{iJ}F^{-1}_{Qr}F^{-1}_{Ls}B^N_Q B^M_L + F_{iJ}F^{-1}_{Qs}F^{-1}_{Lr}B^N_Q B^M_L - \delta_{is}F^{-1}_{Qr}B^N_Q B^M_J - \delta_{ir}F^{-1}_{Qs}B^N_J B^M_Q + \theta^{-1}F_{iJ}\widehat{dB}^{NM}_{rs}\Bigg]\end{aligned} \tag{A.5}$$

where,

$$\widehat{dB}^{NM}_{is} = \frac{1}{V_E}\int_{V_E} JF^{-1}_{Ji}F^{-1}_{Ls}B^N_J B^M_L - JF^{-1}_{Li}F^{-1}_{Js}B^N_J B^M_L dV_0 \tag{A.6}$$

With these definitions in hand the contributions to the residual associated with the first terms of Eq. (3.6) are,

$$\int_{V_0}\frac{\partial\overline{W}}{\partial\overline{F}_{iJ}}\delta\overline{F}_{iJ} + \frac{\partial\overline{W}}{\partial E_I}\delta E_I dV_0 = \delta u_i^N\int_{V_0}\underbrace{\frac{\partial\overline{W}}{\partial\overline{F}_{kJ}}\widetilde{B}^N_{kJi}dV_0}_{R^{u,N}_i} - \delta\phi^N\int_{V_0}\underbrace{\frac{\partial\overline{W}}{\partial E_I}B^N_I dV_0}_{-R^{\phi,N}} \tag{A.7}$$

Then the tangent stiffness is derived from

$$d\left[\int_{V_0}\frac{\partial\overline{W}}{\partial\overline{F}_{iJ}}\delta\overline{F}_{iJ}+\frac{\partial\overline{W}}{\partial E_I}\delta E_I dV_0\right]=\delta u_i^N K_{ij}^{uu,NM}du_j^M+\delta\phi^N K_j^{\phi u,NM}du_j^M+\delta u_i^N K_i^{u\phi,NM}d\phi^M+\delta\phi^N K^{\phi\phi,NM}d\phi^M \tag{A.8}$$

where

$$K_{ij}^{uu,NM}=\int_{V_0}\left(\widetilde{B}_{kLi}^N\frac{\partial^2\overline{W}}{\partial\overline{F}_{kL}\partial\overline{F}_{pQ}}\widetilde{B}_{pQj}^M+\frac{\partial\overline{W}}{\partial\overline{F}_{pQ}}\widetilde{dB}_{pQij}^{NM}\right)dV_0 \tag{A.9}$$

$$K_i^{u\phi,NM}=K_i^{\phi u,MN}=-\int_{V_0}\left(\widetilde{B}_{kLi}^N\frac{\partial^2\overline{W}}{\partial\overline{F}_{kL}\partial E_Q}B_Q^M\right)dV_0 \tag{A.10}$$

$$K^{\phi\phi,NM}=\int_{V_0}B_I^N\frac{\partial^2\overline{W}}{\partial E_I\partial E_J}B_J^M dV_0 \tag{A.11}$$

Each Newton-Raphson iteration then requires the solution of the linear system given by

$$K_{ij}^{uu,NM}du_j^M+K_i^{u\phi,NM}d\phi^M=F_i^{u,N}-R_i^{u,N} \tag{A.12}$$

$$K_j^{\phi u,NM}du_j^M+K^{\phi\phi,NM}d\phi^M=F^{\phi,N}-R^{\phi,N} \tag{A.13}$$

Where $F_i^{u,N}$ and $F^{\phi,N}$ are the standard generalized electromechanical forces given as,

$$F_i^{u,N}=\int_{V_0}b_i N^N dV_0+\int_{S_0}t_i N^N dS_0 \tag{A.14}$$

$$F^{\phi,N}=-\int_{V_0}qN^N dV_0-\int_{S_0}\omega N^N dS_0 \tag{A.15}$$

Appendix B. Critical condition for the onset of wrinkling by a linear elasticity analysis

Here we summarize the linear elasticity analysis by Huang (2005) for wrinkling. In this analysis, we assume the material to be linearly elastic with a shear modulus μ and Poisson's ratio ν. Further assuming no pre-stretch ($\lambda_0=1$), we calculate the change in the elastic strain energy and the electrical energy from the homogeneous state (Fig. 1b) to the wrinkled state with a sinusoidal perturbation to the flat surface (Fig. 1c). At the limit of short wavelength ($\frac{l}{h}\ll 1$), we obtain

$$\Delta U^{elastic}=\frac{k}{4(1-\nu)}\mu A^2 \tag{B.1}$$

$$\Delta U^{electric}=-\frac{k}{4}\varepsilon E_0^2 A^2 \tag{B.2}$$

where $k=\frac{2\pi}{l}$ is the wavenumber, A is the wrinkle amplitude, $E_0=\frac{V}{h}$ is the electrical field in the homogeneous state (before perturbation). The elastic energy in Eq. (B.1) was obtained for an infinitely thick, linearly elastic substrate in the previous studies of thin film wrinkling by many (e.g., Huang et al., 2005).

The total energy change (per unit area of the surface) is:

$$\Delta U=\Delta U^{elastic}+\Delta U^{electric}=\frac{1}{4}k\mu A^2\left(\frac{1}{1-\nu}-\frac{\varepsilon}{\mu}E_0^2\right) \tag{B.3}$$

Thus, the critical condition for the wrinkling instability is obtained by setting $\Delta U=0$, which predicts a critical electrical field:

$$E_W=\sqrt{\frac{\mu}{\varepsilon}\frac{1}{1-\nu}} \tag{B.4}$$

The electrical field in the homogeneous state (before perturbation) depends on the applied voltage and the change of thickness (assuming compressible). For a given voltage, the thickness change from the reference state to the homogeneous state is obtained as

$$\frac{\delta}{h_0}\left(1-\frac{\delta}{h_0}\right)^2=\frac{\varepsilon V^2}{4\mu h_0^2}\frac{1-2\nu}{1-\nu} \tag{B.5}$$

where $\delta=h_0-h$.

At the critical electrical field for the onset of wrinkling, we have

$$\frac{\delta_c}{h_0} = \frac{1}{4}\frac{1-2\nu}{(1-\nu)^2} \tag{B.6}$$

Thus the critical condition in terms of the applied voltage is:

$$V_W = E_W h = h_0\left(\frac{3-6\nu+4\nu^2}{4(1-\nu)^{5/2}}\right)\sqrt{\frac{\mu}{\varepsilon}} \tag{B.7}$$

At the limit of an incompressible material, we have $\nu = 0.5$ and $V_W/h_0 = \sqrt{2\mu/\varepsilon}$, which is identical to Eq. (2.23).

References

Auricchio, F., Beirao da Veiga, L., Lovadina, C., Reali, A., Taylor, R.L., Wriggers, P., 2013. Approximation of incompressible large deformation elastic problems: some unresolved issues. Comput. Mech. 52, 1153–1176.

Biot, M.A., 1963. Surface instability of rubber in compression. Appl. Sci. Res. 12, 168–182.

Cai, S., Chen, D., Suo, Z., Hayward, R.C., 2012. Creasing instability of elastomer films. Soft Matter. 8, 1301–1304.

Cao, Y., Hutchinson, J.W., 2011. From wrinkles to creases in elastomers: the instability and imperfection-sensitivity of wrinkling. Proc. R. Soc. A 468, 94–115.

Diab, M., Zhang, T., Zhao, R., Gao, H., Kim, K.-S., 2013. Ruga mechanics of creasing: from instantaneous to setback creases. Proc. R. Soc. A 469, 20120753.

Gent, A.N., Cho, I.S., 1999. Surface instabilities in compressed or bent rubber blocks. Rubber Chem. Technol. 72 (2), 253–262.

Groh, R.M.J., Pirrera, A., 2019. On the role of localizations in buckling of axially compressed cylinders. Proc. R. Soc. Lond. Ser. A Math. Phys. Eng. Sci. 475 (2224), 20190006.

Hohlfeld, E.B., 2008. PhD thesis. Harvard University, Cambridge, MA.

Hohlfeld, E.B., Mahadevan, L., 2011. Unfolding the sulcus. Phys. Rev. Lett. 106, 105702.

Hong, W., Zhao, X., Suo, Z., 2009. Formation of Creases on the Surfaces of Elastomers and Gels. Appl. Phys. Lett. 95, 111901.

Horak, J., Lord, D.J., Peletier, M.A., 2006. Cylinder buckling: the mountain pass as an organizing center. SIAM J. Appl. Math. 66, 1793–1824.

Huang, R., 2005. Electrically induced surface instability of a conductive thin film on a dielectric substrate. Appl. Rhys. Lett. 87, 151911.

Huang, Z.Y., Hong, W., Suo, Z., 2005. Nonlinear analyses of wrinkles in a film bonded to a compliant substrate. J. Mech. Phys. Solids 53, 2101–2118.

Hutchinson, J.W., 2021. Surface instabilities of constrained elastomeric layers subject to electro-static stressing. J. Mech. Phys. Solids 153, 104462.

Hutchinson, J.W., Huang, R., Landis, C.M., 2022. Errata: Surface instabilities of constrained elastomeric layers subject to electro-static stressing by J. W. Hutchinson. J. Mech. Phys. Solids 153 (2021), 104462.

Kofod, G., Kornbluh, R., Pelrine, R., Sommer-Larson, P., 2003. Actuation response of polyacrylate dielectric elastomers. J. Intell. Mater. Syst. Struct. 14, 787–793.

Koh, S.J.A., Keplinger, C., Li, T.F., Bauer, S., Suo, Z., 2011. Dielectric elastomer generators: how much energy can be converted? IEEE/ASME Trans. Mechatron. 16, 33–41.

Kreilos, T., Schneider, T.M., 2017. Fully localized post-buckling states of cylindrical shells under axial compression. Proc. R. Soc. Lond. Ser. A Math. Phys. Eng. Sci. 473, 20170177.

Mueller-Hoeppe, D.S., Loehnert, S., Wriggers, P., 2009. A finite deformation brick element with inhomogeneous mode enhancement. Int. J. Numer. Methods Eng. 78, 1164–1187.

Park, H.S., Nguyen, T.D., 2013. Viscoelastic effects on electromechanical instabilities in dielectric elastomers. Soft Matter. 9, 1031–1042.

Park, H.S., Suo, Z., Zhao, J., Klein, P.A., 2012. A dynamic finite element method for inhomogeneous deformation and electromechanical instability of dielectric elastomer transducers. Int. J. Solids Struct. 49, 2187–2194.

Park, H.S., Wang, Q., Zhao, X., Klein, P.A., 2013. Electromechanical instability on dielectric polymer surface: Modeling and experiment. Comput. Methods Appl. Mech. Eng. 260, 40–49.

Plante, J.S., Dubowsky, S., 2006. Large-scale failure modes of dielectric elastomer actuators. Int. J. Solids Struct. 43, 7727–7751.

Simo, J.C., Armero, F., 1992. Geometrically non-linear enhanced strain mixed methods and the method of incompatible modes. Int. J. Numer. Methods Eng. 33, 1413–1449.

Stark, K.H., Garton, C.G., 1955. Electric strength of irradiated polythene. Nature 176, 1225–1226.

Tanaka, T., Sun, S.-T., Hirokawa, Y., Katayama, S., Kucera, J., Hirose, Y., Amiya, T., 1987. Mechanical instability of gels at phase transformation. Nature 325, 796–798.

Wang, Q., Tahir, M., Zhang, L., Zhao, X., 2011a. Electro-creasing instability in deformed polymer experiments and theory. Soft Mater 7, 6583–6589.

Wang, Q., Zhang, L., Zhao, X., 2011b. Creasing to cratering instabilities in polymers under ultrahigh electric fields. Phys. Rev. Lett. 106, 118301.

Wang, Q., Zhao, X., 2013. Creasing-wrinkling transition in elastomer films under electric fields. Phys. Rev. E 88, 042403.

Zhao, X., Suo, Z., 2007. Method to analyze electromechanical stability of dielectric elastomers. Appl. Phys. Lett. 91, 061921.